Particles I

Access the latest eBook →

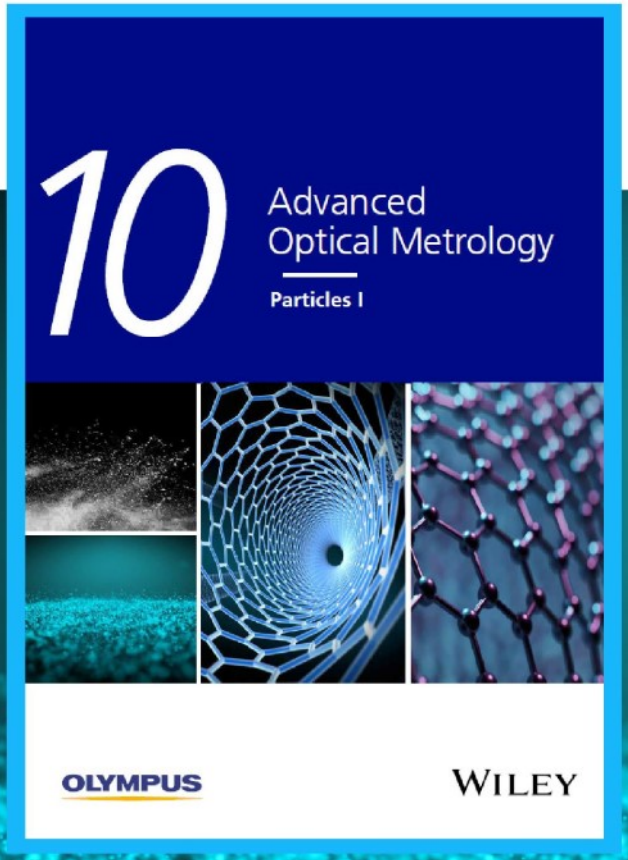

Particles: Unique Properties, Uncountable Applications

Read the latest eBook and better your knowledge with highlights from the recent studies on the design and characterization of micro- and nanoparticles for different application areas.

Access Now

This eBook is sponsored by

OLYMPUS

WILEY

ADVANCED FUNCTIONAL MATERIALS
www.afm-journal.de

From Fully Strained to Relaxed: Epitaxial Ferroelectric $Al_{1-x}Sc_xN$ for III-N Technology

Georg Schönweger, Adrian Petraru, Md Redwanul Islam, Niklas Wolff, Benedikt Haas, Adnan Hammud, Christoph Koch, Lorenz Kienle, Hermann Kohlstedt, and Simon Fichtner**

The recent emergence of wurtzite-type nitride ferroelectrics such as $Al_{1-x}Sc_xN$ has paved the way for the introduction of all-epitaxial, all-wurtzite-type ferroelectric III-N semiconductor heterostructures. This paper presents the first in-depth structural and electrical characterization of such an epitaxial heterostructure by investigating sputter deposited $Al_{1-x}Sc_xN$ solid solutions with x between 0.19 and 0.28 grown over doped n-GaN. The results of detailed structural investigations on the strain state and the initial unit-cell polarity with the peculiarities observed in the ferroelectric response are correlated. Among these, a Sc-content dependent splitting of the ferroelectric displacement current into separate peaks, which can be correlated with the presence of multiple strain states in the $Al_{1-x}Sc_xN$ films is discussed. Unlike in previously reported studies on ferroelectric $Al_{1-x}Sc_xN$, all films thicker than 30 nm grown on the metal (M)-polar GaN template feature an initial multidomain state. The results support that regions with opposed polarities in as-grown films do not result as a direct consequence of the in-plane strain distribution, but are rather mediated by the competition between M-polar epitaxial growth on an M-polar template and a deposition process that favors nitrogen (N)-polar growth.

1. Introduction

Wide and tunable bandgaps, high electron mobility, good breakdown resistance, high thermal stability as well as advanced epitaxial deposition techniques have made the III-N compounds and their heterostructures one of the most successful semiconductor classes.[1] Commercial applications are wide ranging from radio frequency (RF) and power electronics to light emitting diodes (LEDs).[2–4] Current research focuses on extending these applications—next to the trend to expand beyond what are mainly discrete devices to fully integrated III-N solutions, either by integrating, e.g., GaN on CMOS or by developing fully GaN-based complementary circuits.[5–7] As the base technology has thus reached a high maturity, further innovation will require the integration of new compounds with increased functionality. Due to the predominance of the wurtzite-type structure in III-N compounds, its inherent spontaneous polarization is a crucial factor for core applications such as high electron mobility transistors (HEMTs) or LEDs.[8,9] Consequently, increased flexibility or even reconfigurability of the polarization direction will enable powerful new approaches for the continued development of III-N technology. This reconfigurability can readily be obtained through ferroelectricity, which becomes accessible since the formation of III-N based solid solutions such as $Al_{1-x}Sc_xN$ lead to a flattening of the wurtzite-type energy landscape.[10,11] Structurally, this increases the a/c-lattice parameter ratio as well as the internal parameter u (the distance from a metal to a nitrogen atom relative to the c-lattice parameter). Energetically, it will result in a lowering of the energy barrier between the two stable polarization states (metal (M)- and nitrogen (N)-polar, see **Figure 1**), until ferroelectric switching becomes possible by locally transitioning through the intermediate layered hexagonal structure.

G. Schönweger, A. Petraru, H. Kohlstedt
Institute of Electrical and Information Engineering
Kiel University
Kaiserstr. 2, D-24143 Kiel, Germany
E-mail: gmsc@tf.uni-kiel.de

The ORCID identification number(s) for the author(s) of this article can be found under https://doi.org/10.1002/adfm.202109632.

© 2022 The Authors. Advanced Functional Materials published by Wiley-VCH GmbH. This is an open access article under the terms of the Creative Commons Attribution-NonCommercial License, which permits use, distribution and reproduction in any medium, provided the original work is properly cited and is not used for commercial purposes.

DOI: 10.1002/adfm.202109632

M. R. Islam, N. Wolff, L. Kienle, S. Fichtner
Institute for Material Science
Kiel University
Kaiserstr. 2, D-24143 Kiel, Germany
E-mail: simon.fichtner@isit.fraunhofer.de

B. Haas, C. Koch
Institute of Physics & IRIS Adlershof
Humboldt-Universität zu Berlin
Newtonstr. 15, D-12489 Berlin, Germany

A. Hammud
Department of Inorganic Chemistry
Fritz-Haber Institute of the Max-Planck Society
Faradayweg 4-6, D-14195 Berlin, Germany

S. Fichtner
Fraunhofer Institute for Silicon Technology (ISIT)
Fraunhoferstr. 1, D-25524 Itzehoe, Germany

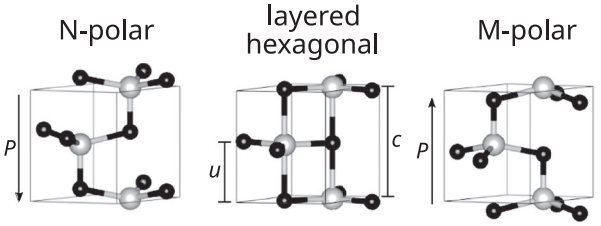

Figure 1. The two stable polarization (*P*) states in ferroelectric $Al_{1-x}Sc_xN$ and the intermediate layered hexagonal structure. Black dots depict nitrogen atoms, grey dots depict Al/Sc atoms.

Therefore, with the advent of wurtzite-type ferroelectrics such as $Al_{1-x}Sc_xN$ and $Al_{1-x}B_xN$ a clear pathway toward a tunable polarization in chemically and structurally matched III-N based material systems has emerged.[12,13] The key toward realizing such all-epitaxial, all-wurtzite-type ferroelectric/semiconductor heterostructures is in the thorough understanding of their structural as well as electrical properties to allow their knowledge driven engineering. Here, we present a detailed study of these properties for $Al_{1-x}Sc_xN$ films with Sc contents of 19, 24, and 28 at% relative to the total amount of metal atoms ($x = 0.19$, 0.24, 0.28) deposited by sputter epitaxy on doped n-GaN/sapphire substrates. In addition to the recently demonstrated ferroelectric switching of epitaxial $Al_{1-x}Sc_xN$ deposited on GaN by molecular beam epitaxy,[14] our study reveals that the interplay between the growth template and the structural properties of the film can lead to previously unknown peculiarities in the ferroelectric response of the $Al_{1-x}Sc_xN$ film which will play a crucial role in understanding the behavior of the spontaneous polarization in epitaxial wurtzite-type ferroelectric/semiconductor heterostructures.

This paper is structured into three sections, starting with a detailed structural characterization of our films using sophisticated techniques of X-ray diffraction (XRD) and dedicated scanning transmission electron microscopy (STEM), followed by the characterization of the ferroelectric response and finally an in-depth analysis of the initial polarization domain state of the samples.

The first section includes reciprocal space mappings (RSM) to confirm phase purity and epitaxial relationships, (a)symmetric XRD scans to deduce the $Al_{1-x}Sc_xN$ lattice parameters in dependence of Sc content and films thickness as well as complementary scanning nano-beam electron diffraction (NBED) maps of the strain distribution to illustrate the evolution of film strain at close to nm-resolution. Section 2 details the overall ferroelectric response of the films via polarization/displacement-current measurements in dependence on the electric field. Measurements are compared for the three different Sc contents and film thicknesses between 30 and 300 nm. The results are discussed on the basis of the microstructure as presented in Section 1. Finally, the as-deposited polarity of the $Al_{1-x}Sc_xN$ films is revealed to be strongly influenced by the interplay between the M-polar GaN template and a deposition process promoting N-polar films. The existence of horizontal inversion domain boundaries in $Al_{0.72}Sc_{0.28}N$ films with thicknesses above 30–40 nm is suggested by unipolar ferroelectric switching experiments and is supported by atomically resolved STEM to image the structure polarity in as-deposited, vertically separated regions of the film as well as by etching experiments.

2. Structural Characterization

Complementary structural characterization methods were employed to elucidate whether and to what degree the deposited $Al_{1-x}Sc_xN$ films are grown epitaxially on GaN templates and to what extent the GaN interface influences the local and average strain and orientation of the thin film—which could ultimately have a significant impact on the ferroelectric properties of the film. To investigate the quality of epitaxial growth, wide-range RSM of $Al_{1-x}Sc_xN/GaN/Al_2O_3$ heterostructures have been recorded on a laboratory-based diffractometer. $Al_{0.72}Sc_{0.28}N$ films with thicknesses ranging from 10 up to 300 nm as well as 100 nm thick $Al_{1-x}Sc_xN$ films with Sc contents of 19 and 24 at% were analyzed to understand the in-plane epitaxial strain distribution, whose analysis is complemented by scanning NBED derived strain maps of the 300 nm thick $Al_{0.72}Sc_{0.28}N$ film.

RSM provide a 2-dimensional representation of the *k*-space revealing the crystallographic relations of the $Al_{1-x}Sc_xN$ films to those of the underlying buffer layer and substrate. A wide-range RSM of a 300 nm thick $Al_{0.72}Sc_{0.28}N$ film, representative for our heterostructures, is shown in **Figure 2**.

All present reflections were identified and attributed to the $Al_{0.72}Sc_{0.28}N$ thin film (marked in yellow), the GaN buffer layer (marked in black), and the Al_2O_3 substrate (marked in red). Thus, we identify one crystallographic phase in our $Al_{1-x}Sc_xN$ films, which is the polar wurtzite-type phase (space group 186, $P6_3mc$) responsible for the ferroelectricity of the material. The films have been grown epitaxially on the underlying 4 µm thick doped n-GaN template, with no significant contribution from randomly oriented volume. They have thus the same crystallographic orientation as the GaN films, with the *c*-axis pointing out-of-plane and parallel hexagonal (0001) basal planes.

The in-plane epitaxial relationship between Al_2O_3, GaN, and $Al_{0.72}Sc_{0.28}N$ is also revealed by the pole figure measurement presented in **Figure 3**, showing almost coinciding 01–13 reflection intensities.

Thus, the epitaxial relationship between film and template is as expected: [1-100](0001)$Al_{1-x}Sc_xN$ ‖ [1-100](0001)GaN. The in-plane relation of the lattice orientation of GaN and sapphire is [1–100](0001)GaN ‖ [11–20](0001)Al_2O_3, meaning a 30° in-plane rotation of the GaN with respect to the Al_2O_3, as visible in the pole figure and reported also in literature.[15] In addition to the low resolution wide-range RSM, high-resolution data was obtained to determine the lattice parameters of the films more accurately and draw conclusions on their strain state. The *c*-lattice parameter of the $Al_{1-x}Sc_xN$ films could be obtained for film thicknesses down to 20 nm from the high-resolution specular scans using a two-bounce monochromator. For *a*-lattice parameter determination down to 30 nm film thickness, high-resolution asymmetric scans of non-specular 10–15, as well as –1013 reflections, were recorded. The in-plane rotation of the columnar grains with respect to each other was analyzed by high-resolution in-plane rocking curve (RC) scans using a two-bounce monochromator. We would like to mention here that the symmetric and asymmetric scans represent an average over the whole film thickness. Thus, the obtained lattice-parameters for films with epitaxially strained- as well as relaxed regions reflect an average of the present strain states. The in-plane RC measurements were performed at an incidence angle of about

© 2022 The Authors. Advanced Functional Materials published by Wiley-VCH GmbH

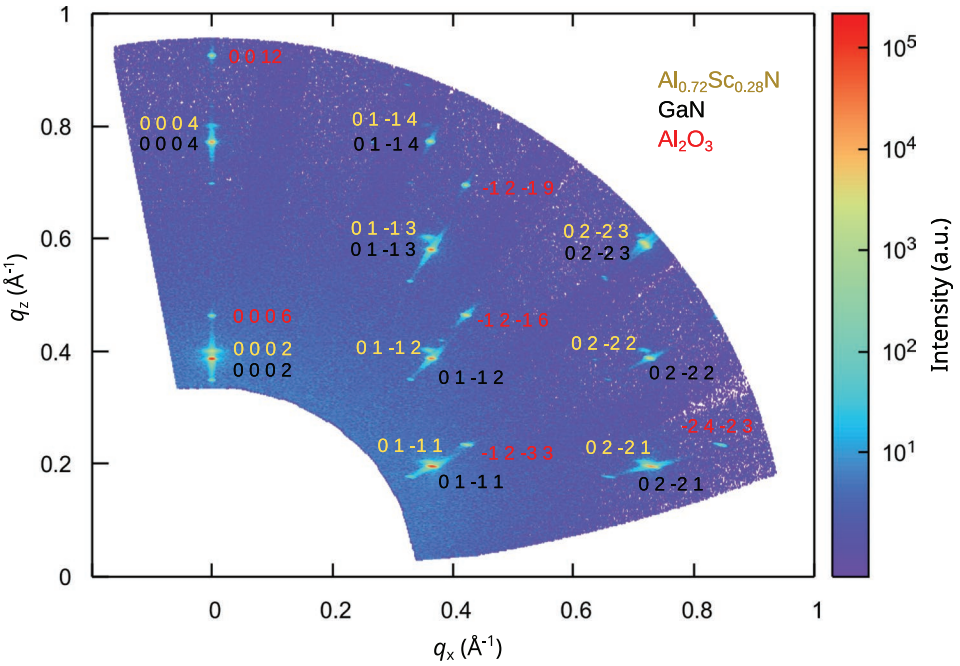

Figure 2. Wide-range RSM of the $Al_{0.72}Sc_{0.28}N$ (300 nm)/n-GaN/Al_2O_3(substrate) heterostructures. The intensities corresponding to Al_2O_3, GaN, and $Al_{0.72}Sc_{0.28}N$ are denoted respectively in red, black, and yellow. All non-labeled spots correspond to Cu K-beta (k_b) reflections.

0.3°, making them surface sensitive. Therefore, in this particular case, only a thin, surface near region was analyzed.

In **Figure 4**a, the evolution of the *a*-lattice parameter of 100 nm thick $Al_{1-x}Sc_xN$ is depicted for different Sc concentrations. With decreasing Sc content, the *a*-lattice parameter of $Al_{1-x}Sc_xN$ is decreasing and approaches the *a*-lattice parameter of GaN at 19 at% Sc. This decrease of the *a*-lattice parameter is expected due to the difference in preferred coordination and atomic radii between Al and Sc atoms, which is known to lead to a diminution of the wurtzite basal plane.[10,11] For epitaxial systems, a smaller *a*-lattice misfit between the film and the substrate leads to a higher critical thickness, meaning the transition from a fully strained epitaxial to a relaxed film shifts to a higher thickness. Thus, when decreasing the Sc content starting from 28 at%, the critical thickness is expected to increase until being infinite at 18 at% Sc due to lattice-matching with the GaN.[16] Hence, for a 100 nm thick film at 19 at% Sc, a uniform lattice without a significant strain gradient is expected. To study the in-plane strain state of the nearly lattice-matched film in more detail, a high-resolution RSM of the 10–15 reflections was recorded for 100 nm thick $Al_{0.81}Sc_{0.19}N$, as shown in Figure 4b. Both the 10–15 $Al_{0.81}Sc_{0.19}N$ and the 10–15 GaN reflections are distributed almost congruently on (q_x/q_z) space with their maxima located at identical q_x position, which also confirms that the $Al_{0.81}Sc_{0.19}N$ is in-plane lattice-matched to the GaN template.

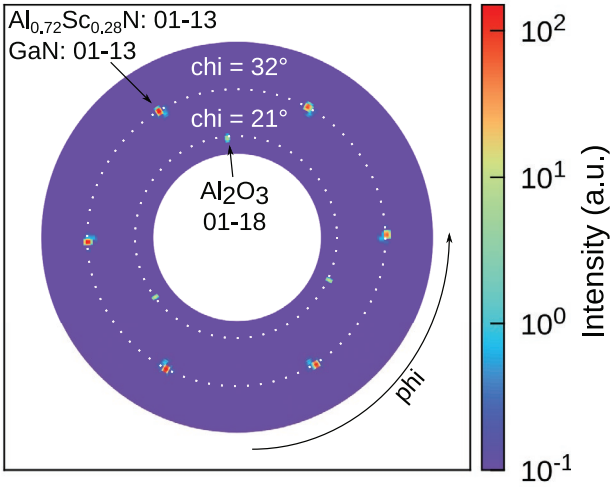

Figure 3. Pole figure of the 01–13 reflections from $Al_{0.72}Sc_{0.28}N$ (300 nm)/n-GaN/Al_2O_3(substrate) heterostructures.

A minor increase in the *c*-lattice parameter is observed while increasing the Sc content, as illustrated in Figure 4a. In relaxed films deposited on Si, an increase of the *c*-lattice parameter with lower Sc concentration was observed.[17] In the present case, the *c*-lattice parameter changes also due to elastic deformation of the unit cell imposed by the epitaxial strain which superimposes the change of the *c*-lattice parameter due to Sc variation.

Structural analysis of a thickness series of non-lattice-matched $Al_{0.72}Sc_{0.28}N$ films allows us to understand the strain relaxation in more detail. In this context, Figure 4c illustrates the *a*- and *c*-lattice parameter variation in dependence of the $Al_{0.72}Sc_{0.28}N$ film thickness. When reducing the film thickness, the *a*-lattice parameter is observed to be decreased until being close to be lattice-matched with the in-plane lattice of the GaN template. Thus, below ≈50 nm, $Al_{0.72}Sc_{0.28}N$ films appear to be fully strained to the GaN template. Between 40 and 100 nm, a steep increase of *a*-lattice parameter is observed, followed by a more constant plateau above 100 nm film thickness. Therefore, in-plane lattice relaxation occurs within a thickness range between 40 nm and 100 nm for 28 at% Sc. Using an energy

© 2022 The Authors. Advanced Functional Materials published by Wiley-VCH GmbH

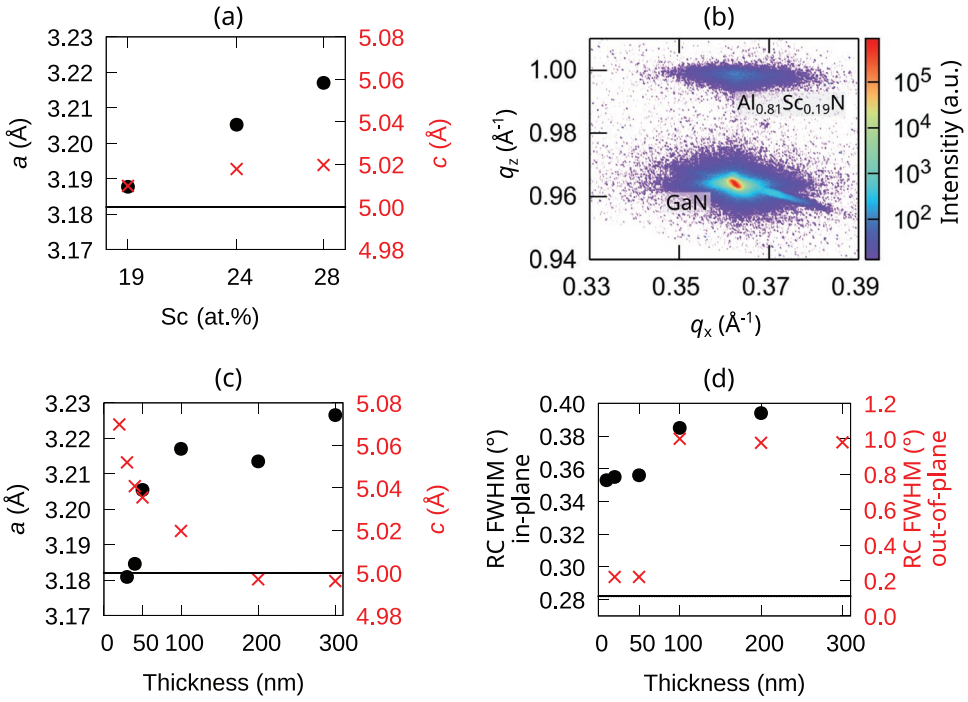

Figure 4. a) Evolution of *a*- and *c*-lattice parameters of 100 nm thick $Al_{1-x}Sc_xN$ in dependence of Sc content. b) High-resolution reciprocal space mapping of $Al_{0.81}Sc_{0.19}N$ 10-15 reflection. c) *a*- (black) and *c*-lattice parameter (red) of $Al_{0.72}Sc_{0.28}N$ films in dependence of film thickness. d) The corresponding FWHM of the 0002 RC (out-of-plane) and FWHM of the 10–10 RC (in-plane). For comparison the measured *a*-lattice parameter, as well as the measured FWHM of the 10–10 RC (in-plane) of the GaN, is illustrated as a solid black line in (a), (c), and (d), respectively. For lattice parameter determination we estimate an error of 1 pm.

balance model, the critical thickness for $Al_{1-x}Sc_xN$/GaN heterostructures was previously calculated to be ≈70 nm for 28 at% Sc.[16] Considering an estimated error for Scandium concentration determination in our films of 2 at%, this is in good agreement with the experimentally found critical thickness of ≈40 nm. By plotting the full-width at half maximum (FWHM) of the in-plane and out-of-plane rocking curves over the film thickness, as depicted in Figure 4d, a clear step is observed between 50 and 100 nm, thus providing yet more support that the transition from a fully strained to a partially relaxed lattice occurs at around 50 nm film thickness. At this particular thickness, the FWHMs of the rocking curves measured for in- and out-of-plane configurations change by 10% and 400%, respectively. Hence, a fully strained thin film below this transition regime exhibits an improved in-plane and out-of-plane alignment (tilt) of its nanoscale columnar grains. Noticeably, the in-plane mosaicity of our sputtered films is comparable to the GaN template itself with its in-plane FWHM of the rocking curve of 0.28°.

To complement the XRD measurements, we employed STEM imaging in combination with scanning NBED to resolve the local strain evolution with close to nm resolution on a 300 nm thick $Al_{0.72}Sc_{0.28}N$ film. STEM and electron diffraction (not shown) investigations confirm the results obtained by XRD on the epitaxial growth of the $Al_{1-x}Sc_xN$ films. As has to be expected from a sputtered film deposited at comparably low temperatures, the films do not form a single crystal but rather adjacent columnar grains with diameters in the range of < 10 nm in the nucleation zone expanding to about 20 nm at the top of the film (see **Figure 5**a). Despite epitaxial growth conditions providing a rigid in-plane orientation with sixfold symmetry, STEM imaging reveals that the individual columnar grains are presumably randomly in-plane rotated with respect to each other by about 20–30 mrad—as it is also apparent through the finite mosaicity of the films depicted in Figure 4d.

The powerful combination of STEM providing atomic resolution information and scanning NBED offering precise structural information was applied to the material system. From the nano-beam diffraction data, both in-plane (ε_{xx}) and out-of-plane (ε_{zz}) components of the strain matrix were calculated to determine the internal strain distribution from the interface toward the surface, including the related critical thickness for the film to relax from its fully strained state.

A cross-sectional view onto the $Al_{0.72}Sc_{0.28}N$(300 nm)/n-GaN layer structure is displayed in the annular bright-field (ABF) STEM image of Figure 5a and shows the aforementioned columnar character of the $Al_{0.72}Sc_{0.28}N$ film and extended vertical defects within the GaN buffer layer, which likely originate from the heavy doping of the n-GaN or its growth conditions on the sapphire substrate. The GaN polarity was determined to be M-polar at all examined positions left, right and in between the defects as indicated in the inset showing a high-resolution ABF STEM micrograph of the atomic structure of GaN.

Figure 5b displays a virtual dark-field (VDF) image of the scanning NBED experiment and the corresponding quantified strain maps and averaged profiles of the in-plane and out-of-plane components, both showing the local strain distribution

© 2022 The Authors. Advanced Functional Materials published by Wiley-VCH GmbH

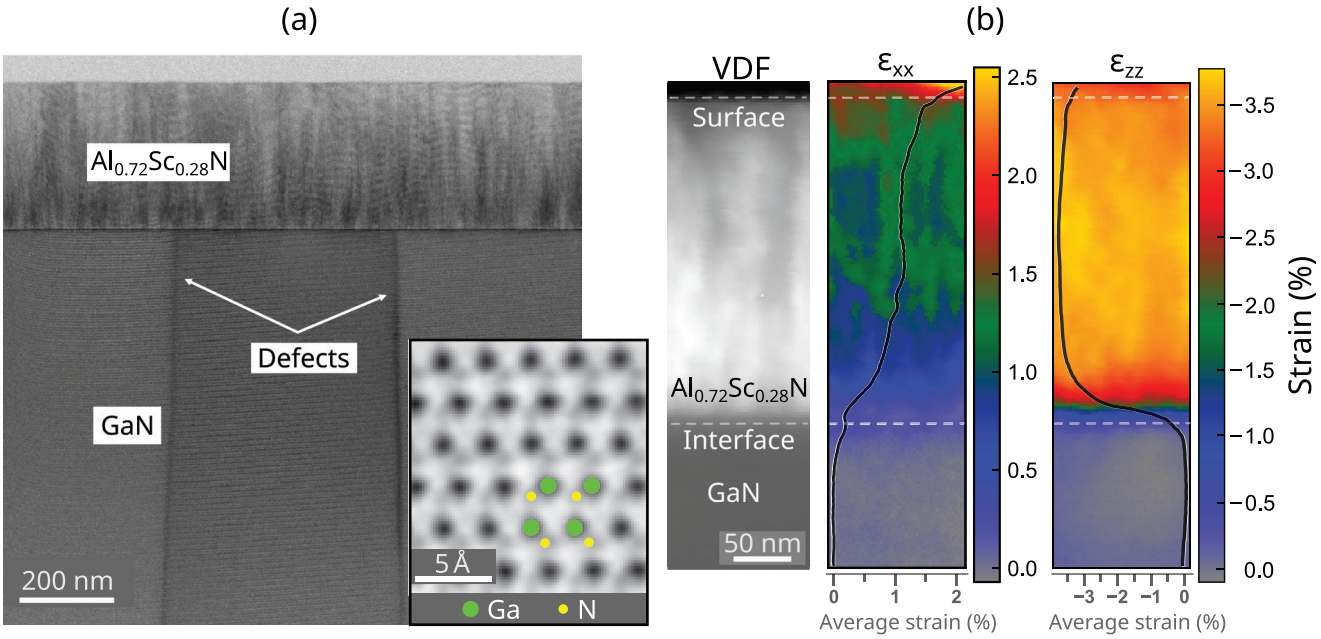

Figure 5. a) ABF STEM overview image of the $Al_{0.72}Sc_{0.28}N$/n-GaN layers showing the columnar grain structure within the $Al_{0.72}Sc_{0.28}N$ film and extended defects in the GaN single crystalline template. The inset shows an atomic resolution ABF STEM image of GaN and verifies its M-polar orientation (green: Ga atoms, yellow: N atoms). b) Virtual dark-field (VDF) image of the scanning NBED experiment and strain maps of the ε_{xx} and ε_{zz} strain components calculated in reference to the GaN template for the $Al_{0.72}Sc_{0.28}N$ film.

probed across the entire 300 nm $Al_{0.72}Sc_{0.28}N$ film in reference to the GaN buffer layer. The experimental resolution of about 5 nm limited the accuracy in determining the position of the interface to ±5 nm which was placed at the onset of rising material contrast in the VDF image. The in-plane strain component was calculated from the array of [11–20] diffraction patterns describing the distance between the (01–10) planes. From the bulk of the GaN (zero strain, reference), the strain value is observed to monotonously increase when approaching the interface, forming a small plateau of ≈0.2% strain. On the $Al_{0.72}Sc_{0.28}N$ side of the interface, the in-plane strain distribution forms a plateau within the first ≈30 nm with an average of 0.2% strain. With increasing thickness, the average strain distribution continues to increase slowly over a range of ≈80 nm up to 1.2%, where a second plateau starts to appear up to a thickness of ≈250 nm. This plateau at 1.2% strain corresponds to an *a*-lattice parameter of 3.22 Å (considering the measured *a*-lattice parameter of the GaN bulk corresponding to zero strain), which is in good agreement with the measured *a*-lattice parameter of 3.23 Å for 300 nm thick $Al_{0.72}Sc_{0.28}N$ via asymmetric XRD scans, whereas the latter represents an *a*-lattice parameter averaged over the whole thickness. Further relaxation to a value of 1.5% strain takes place within a range of ≈50 nm below the surface. Even higher values of strain beyond the surface are regarded as artifacts. The observed slow strain relaxation behavior of the in-plane lattice is in strong contrast to the rapid relaxation of the non-clamped *c*-lattice parameter, which tends to be fully relaxed after the first ≈50 nm from the interface.

In summary, all our $Al_{1-x}Sc_xN$ films can be expected to contain a fully strained region close to their n-GaN interface (Figure 5). The extent of this fully strained region is expected to decrease with increasing film thickness—so that for 300 nm it is considerably lower than the critical thickness of ≈40 nm which was determined via XRD measurements. The latter also reveals that films thinner than ≈40 nm are fully strained to the GaN substrate over their entire thickness.

3. Electrical Characterization

The foremost goal of the electrical characterization of our samples was to determine if they are ferroelectric and how their ferroelectricity compares to those films deposited on the common polycrystalline metal interfaces.[12,17] Displacement current density measurements in dependence of the electric field (*J–E* measurements) are at the core of ferroelectric characterization and were performed on capacitors with different $Al_{0.72}Sc_{0.28}N$ film thicknesses as well as different Sc concentrations with a constant thickness of 100 nm. If not stated otherwise, the contacted pad size was 50 × 50 µm^2 and the measurement frequency 1.5 kHz.

Figure 6a shows *J–E* and polarization over the electric field (*P–E*) loops to demonstrate clear ferroelectric switching for a 300 nm thick epitaxial $Al_{0.72}Sc_{0.28}N$ film deposited on doped n-GaN.

Additionally, ferroelectric switching is confirmed by strain over electric field measurements depicted in Figure 6b as well as capacitance over electric field measurements depicted in Figure S1 (Supporting Information). Leakage currents start to appear around E_c, similar to what is seen for highly textured non-epitaxial films on Pt/Si.[17] To separate leakage from switching current, we make use of dynamic leakage current compensation (DLCC).[18] Especially in thin $Al_{1-x}Sc_xN$ films, the

© 2022 The Authors. Advanced Functional Materials published by Wiley-VCH GmbH

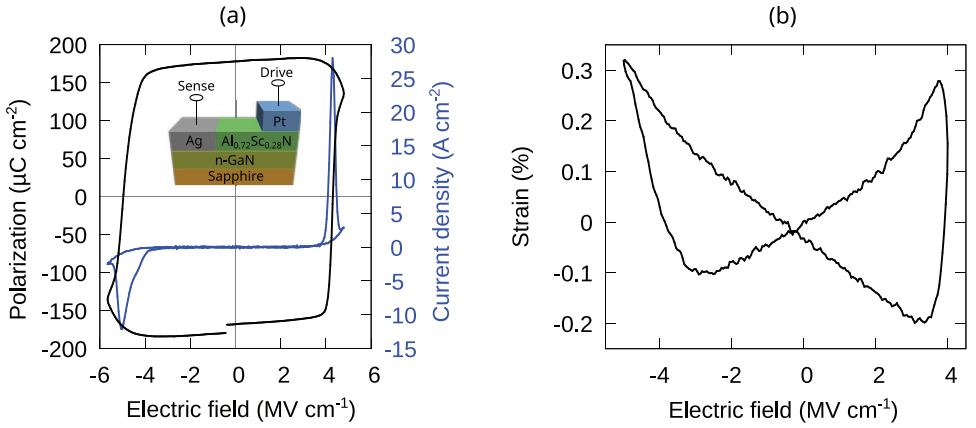

Figure 6. a) *J–E* and *P–E* loop for 300 nm thick $Al_{0.72}Sc_{0.28}N$ on n-GaN measured on a 100 × 100 µm² pad. The inset shows the layer structure and the electrical connections. b) Strain response in dependence of the applied electric field of 200 nm thick $Al_{0.72}Sc_{0.28}N$ on n-GaN measured at 711 Hz.

leakage currents for switching cycles are higher than for non-switching cycles. Therefore, it is typically not possible to fully compensate leakage currents by using positive-up negative-down (PUND) measurements as well as modified DLCC[12]—since both methods compensate using non-switching cycles. In DLCC, leakage is compensated using two successive switching cycles at different frequencies, thus overcoming the aforementioned issue. Therefore, DLCC better reflects the electrical features of our films. This comes however at the price of overlapping switching peaks due to the frequency dependence of the latter, which can lead to the minor artificial negative current response observed under positive fields, as visible in **Figure 7**b. In Figure 7a,b, DLCC *P–E* and *J–E* loops for different $Al_{0.72}Sc_{0.28}N$ film thicknesses are depicted. Although DLCC is not able to fully compensate for the leakage on the positive side, the remanent polarization (P_r) can be approximately determined from the negative half-cycle in Figure 7a. P_r values of roughly 125 µC cm^{-2} are in line with what is known from highly textured $Al_{1-x}Sc_xN$ on Pt/Si for similar Sc concentrations.[12]

Somewhat unexpected—and different to what has been previously observed in $Al_{1-x}Sc_xN$, the data displayed in Figure 7b reveals a broadening of the switching regime including the appearance of two peaks during sweeping negative half-cycles. From frequency-dependent measurements (see Figure S2, Supporting Information), both peaks behave like ferroelectric switching peaks—as expected, with increasing frequency the peak-heights are increasing as well as the peak centers are shifting to higher absolute fields. More gradual switching is also apparent during the negative half-cycle of the butterfly-shaped strain over the electric field loop displayed in Figure 6b, which gives additional evidence that both peaks are of ferroelectric origin. The clear observation of the double-switching phenomenon in our samples was facilitated by contacting the capacitor through the n-GaN, which results in an asymmetric current response that widens the negative side, especially for thinner films. This broadening of the displacement current peaks also occurs during switching two neighboring capacitors in series, i.e., by using the substrate for the series connection and therefore ruling out the influence of the Ag/n-GaN contact (see Figure S3, Supporting Information). Thus, although being highly doped, we expect a voltage drop on a built-up space charge region at the $Al_{1-x}Sc_xN$/n-GaN interface (a more detailed possible explanation for this observation is given at the end of this section). Due to the establishment of this space charge region, peak splitting effects are getting more pronounced with decreasing film thickness down to 100 nm. Below 50 nm, "peak

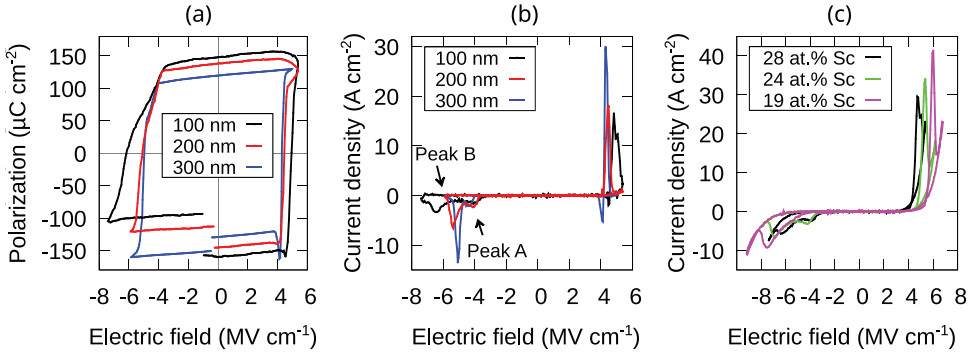

Figure 7. a) DLCC (1 kHz) *P–E* loops and b) corresponding DLCC (1 kHz) *J–E* curves for 100 nm (black), 200 nm (red), and 300 nm (blue) thick $Al_{0.72}Sc_{0.28}N$ films. Leakage compensation was calculated from measurements at 1 and 2 kHz. c) Uncorrected *J–E* curves showing the evolution of the double peak feature during the negative half-cycle for 100 nm thick $Al_{1-x}Sc_xN$ with varying Sc concentrations.

© 2022 The Authors. Advanced Functional Materials published by Wiley-VCH GmbH

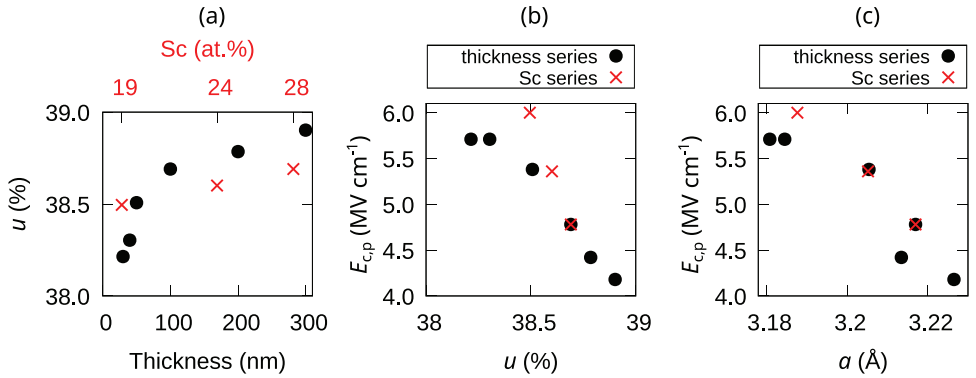

Figure 8. a) Internal parameter u in dependence of $Al_{0.72}Sc_{0.28}N$ film thickness and in dependence of Sc content for 100 nm thick $Al_{1-x}Sc_xN$. b) Positive coercive field ($E_{c,p}$) dependence on the internal parameter u and c) on the a-lattice parameter.

A" shrinks and finally disappears at 30 nm (see Figure S4, Supporting Information). As discussed in Section 2, $Al_{0.72}Sc_{0.28}N$ films with up to ≈40 nm thickness are fully strained to the GaN. Films with thicknesses in between ≈40 and 300 nm consist of a fully strained as well as a more relaxed volume. Since double peaks are only present in films thicker than 30 nm, we expect that they are related to the different strain regimes within the films. To further confirm that the switching peaks are indeed related to different strain regimes, the 100 nm thick samples with 24 at% Sc and 19 at% Sc were investigated. The a-lattice parameter and therefore the in-plane misfit to GaN is decreasing with decreasing Sc content and finally almost matches the GaN a-lattice parameter at 19 at% Sc, as discussed in Section 2. In Figure 7c J–E curves for the 100 nm thick $Al_{1-x}Sc_xN$ with different Sc concentrations are compared. It is evident that for 24 at% Sc "peak A" is shrinking at the cost of "peak B" while finally only one switching peak appears for the uniform fully strained 19 at% Sc film. Due to the compressively strained in-plane lattice of $Al_{1-x}Sc_xN$ at the GaN interface, it is reasonable to conclude that this volume fraction is switched at higher absolute electric fields, as it is known that compressive strain in $Al_{1-x}Sc_xN$ leads to higher coercive fields.[12] Therefore we expect "peak B" to be responsible for switching polarization of the fully strained region near the GaN interface and "peak A" to be responsible for switching the more relaxed region at lower absolute electrical fields. Since at 24 at% Sc the ratio between fully strained and relaxed volume is changing, also the area ratio of the two switching peaks is changing. Furthermore, the lower Sc content causes a higher coercive field, as it can be seen especially for the $Al_{0.81}Sc_{0.19}N$ film. As discussed in Section 2, the high-resolution RSM of the latter film (Figure 4b) is indicative of a largely uniform lattice over the entire film thickness, which can explain the occurrence of only one switching peak. Additional measurements that confirm that the switching behavior described above occurs independent of sample area and measurement setup are given in the supplement.

In order to investigate the effect of epitaxial strain on the coercive field, the internal parameter u was calculated according to $u = a^2/3c^2 + 0.25$[19–21] and is illustrated in **Figure 8**a for the various films investigated in this study. Due to the asymmetric voltage drop at the $Al_{1-x}Sc_xN$/GaN interface, only the positive coercive field ($E_{c,p}$) can be clearly determined and considered for the following evaluations.

As expected, u is decreasing with decreasing film thickness due to the compressively strained $Al_{0.72}Sc_{0.28}N$ close to the GaN interface. As previously shown, a reduction in Sc content leads to a drop in u as well.[10] In our particular case, the effect of epitaxial strain superimposes the distortion of the lattice due to Sc variation, resulting in relatively small changes for the different Sc concentrations. In Figure 8b the coercive field is correlated to the internal parameter u. Clearly, a decrease of the coercive field with increasing u is observed for both series due to a flattening of the energy landscape which facilitates ferroelectric switching.[12] Noticeably, the coercive field changes from 4.2 up to 5.7 MV cm^{-1} for $Al_{0.72}Sc_{0.28}N$ only as an effect of epitaxial strain. Although the trend is clear, a slightly different dependence of $E_{c,p}$ on u is observed for the thickness and the Sc series. This supports the assumption that u alone does not determine the coercive field. Besides distorting the lattice, Sc has an additional effect on the switching behavior, e.g., an introduction of local structural instability which facilitates switching.[22] Contrarily, the coercive field dependence on the a-lattice parameter is more congruent for the two series, as depicted in Figure 8c. To conclude, the coercive field is heavily influenced by epitaxial strain. Additional studies should therefore be conducted to investigate if the systematic introduction of epitaxial tensile strain can be used to further separate the coercive field from the onset of the leakage current.

To provide a possible explanation for the establishment of a space charge region under large negative fields, we rely on the following observation: The onset of the switching current occurs at roughly the same field for both polarities. This observation indicates that there is no large-scale depletion zone in the n-GaN and thus no space charge region at this point. For positive fields, there will be no additional depletion since the n-GaN is biased in the forward direction. For negative fields (and N-polar $Al_{1-x}Sc_xN$), the interface between the ferroelectric and the n-GaN will provide electrons from the charges screening the polarization of the ferroelectric. As soon as polarization switching occurs, this reservoir of charges will be substantially reduced through the rearrangement of the screening charges. Locally, there will no longer be sufficient screening charges to build up a field as high as the coercive field of $Al_{1-x}Sc_xN$. Therefore, the n-GaN will start to deplete when the first regions with M-polarity are formed and the remaining switching current will appear widened due to the additional voltage-drop over the depleted GaN.

© 2022 The Authors. Advanced Functional Materials published by Wiley-VCH GmbH

4. Investigation of the Initial Film Polarity

The polarity of III-N heterostructures is of fundamental importance for, e.g., the carrier type in 2-dimensional electron gases (2DEGs) that form at their polarization discontinuities as well as their etching rate and selectivity—both of which are crucial from the integration point of view.[9,23] Sputtering of $Al_{1-x}Sc_xN$ usually favors N-polar growth, while most III-N heterostructures feature M-polar surfaces. Therefore, the as-deposited polarity of $Al_{1-x}Sc_xN$ grown on top of M-polar GaN is of special interest. To investigate the as-deposited polarity of the films, two successive unipolar triangular excitation signals at 1.5 kHz were applied on pristine pads. This allows distinguishing between switching (first signal, orange) and non-switching (second signal, green) currents, as depicted in **Figures 9**a,b for a 100 nm thick $Al_{0.72}Sc_{0.28}N$ film. Clear current peaks during positive and negative voltage sweeps are visible, meaning there are M-polar as well as N-polar regions inside the same, as-deposited film—unlike in the exclusively N-polar films deposited by similar processes on metal electrodes.[24]

Measurements of the piezoelectric coefficient $d_{33,f}$ on as-deposited pads in comparison to $d_{33,f}$ measured on pads with prior switching to full N-polarity by applying a field above the positive coercive field confirm the as-deposited multipolar state: The as-deposited $d_{33,f}$ for a 200 nm thick $Al_{0.72}Sc_{0.28}N$ capacitor is 19.4% smaller than after switching the same capacitor to full N-polarity. Furthermore, by looking at the full loop of the 100 nm film depicted in Figure 9a, it is apparent that the switching dynamics are completely different for the first unipolar excitation signal. This might not be related to a wake-up effect,[25] but rather an effect of the depleting GaN in the presence of M-polar AlScN and large negative electric fields, as explained in Section 3. The growth of M-polar $Al_{1-x}Sc_xN$ is promoted via the M-polar GaN template. This template-dependent polarity has also been observed for GaN grown by MOCVD—GaN grows N-polar on non-polar sapphire and M-polar on a template that exhibits M-polarity (AlN/sapphire).[26] For thicknesses $\gtrsim$40 nm, the film undergoes a transition to N-polarity, in accordance with the preference of the deposition process. This thickness-related transition from M- to N-polarity is confirmed by thickness-dependent as-deposited unipolar measurements, as depicted in Figure 9c. With decreasing film thickness the M-polar switching peak area is increasing, meaning the N-polar volume portion is shrinking. This increase in polarization when reducing the thickness of the non-switching layer is a common feature of dielectric/ferroelectric heterostructures.[27] Unipolar measurements on thinner as-deposited $Al_{0.72}Sc_{0.28}N$ films reveal full M-polarity for 30 nm film thickness, while at 40 nm film thickness a switching peak confirming the presence of N-polarity is observed (see Figure S5, Supporting Information). This confirms the aforementioned transition from M- to N-polarity at a thickness between 30 and 40 nm. Since also films with lower Sc concentrations and thus reduced built-in stress exhibit M- and N-polar as-deposited regions (see Figure S6, Supporting Information), we conclude that their presence is not predominantly related to the strain relaxation that is also observed to start at around 40 nm film thickness, but rather an independent effect due to the influence of the M-polar GaN at the interface. Conversely, the change in polarity necessarily induces an extended lateral defect (i.e., the domain wall), which might be the origin for the commencing stress relaxation at this particular thickness. To visualize the extent of the as-deposited M-polarity, etching experiments were conducted and are illustrated in **Figure 10**, since etchants like Phosphoric acid (H_3PO_4) are highly selective to the polarity of wurtzite-type crystals.[23] After switching the

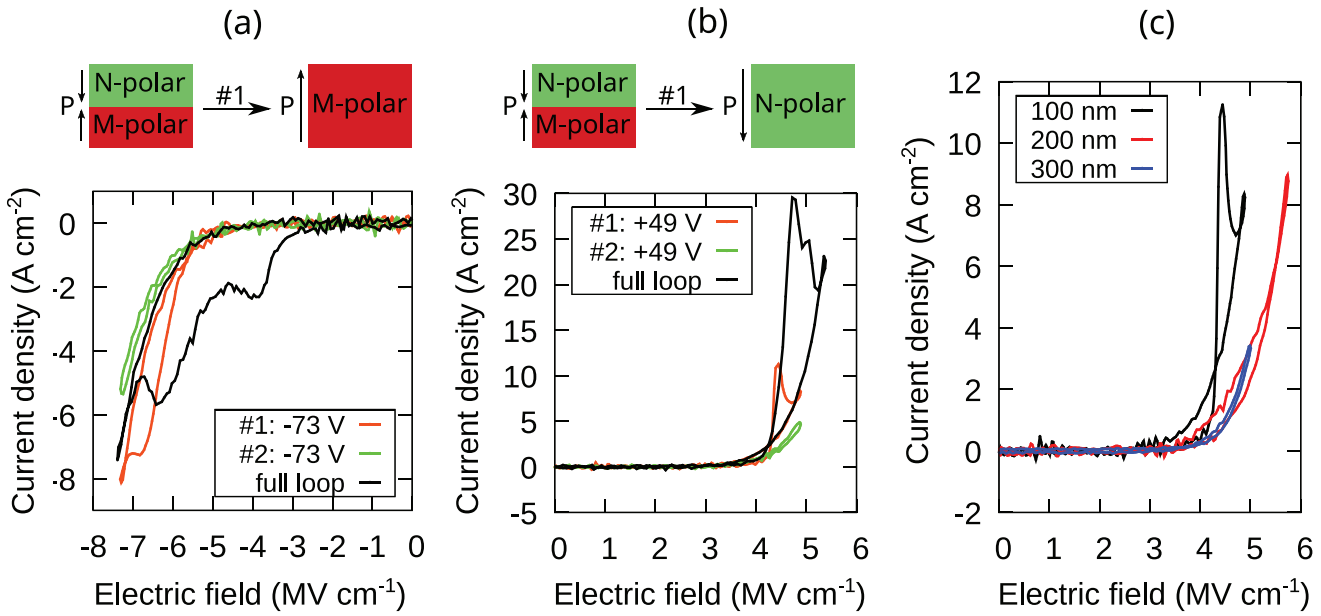

Figure 9. a) Negative and b) positive unipolar measurements on pristine 100 nm $Al_{0.72}Sc_{0.28}N$ capacitors to visualize the as-deposited polarization. The sketches above the respective figures represent the $Al_{1-x}Sc_xN$ polarization state before and after the first applied unipolar voltage. The *J*–*E* half-cycle after fully switching the same film to the respective opposite polarity is depicted in black c) Positive unipolar measurements on pristine $Al_{0.72}Sc_{0.28}N$ capacitors in dependence of film thickness to illustrate the extent of as-deposited M-polarity.

© 2022 The Authors. Advanced Functional Materials published by Wiley-VCH GmbH

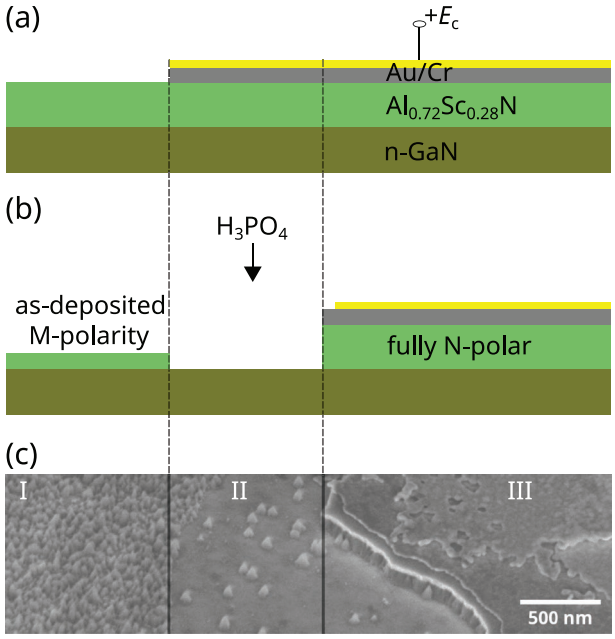

Figure 10. a) Schematic cross-section of a patterned Au(10 nm)/Cr(30 nm)/$Al_{0.72}Sc_{0.28}N$(100 nm)/n-GaN heterostructure with positive coercive field applied to the capacitor. b) Expected cross-section after removing part of the top-electrode and subsequent etching in phosphoric acid c) Scanning electron microscopy (SEM) image of the etched heterostructure sketched in (b). The three expected topographies marked with I, II, and III are clearly visible.

100 nm thick $Al_{0.72}Sc_{0.28}N$ below the patterned top-electrode to full N-polarity, as sketched in Figure 10a, the top electrodes were partially removed by wet-etching. Subsequent to the etching in 80 °C H_3PO_4, the etch-profile sketched in Figure 10b is expected and observed experimentally, as depicted in Figure 10c.

In region I, the as-deposited residual M-polar $Al_{0.72}Sc_{0.28}N$ volume fraction is visualized, followed by a clear transition to the neighboring almost fully etched region II, which was previously switched to full N-polarity. Noticeably, the topography in region I exhibits a rather complex three-dimensional structure. We presume the rough surface structure is a consequence of the M- to N-polarity transitions in the as-grown film taking place at different levels for the respective columnar $Al_{1-x}Sc_xN$ nanograins. In region II, only cone-like residuals on a very smooth surface are visible. These cone-like residuals are characteristic for N-polar $Al_{1-x}Sc_xN$, while the very smooth surrounding surface is indicative of an etch-stop at the $Al_{1-x}Sc_xN$/GaN interface.[23] The smooth etch-stop on the GaN surface allows the conclusion that the latter is not switched to N-polarity to a significant extend. This observation also gives additional support to our explanation that the double switching peak phenomenon originates in the $Al_{1-x}Sc_xN$ and is not a consequence of partial switching in GaN.

To further support this discussion, we confirmed the expected location of the M- and N-polar regions in the as-deposited $Al_{0.72}Sc_{0.28}N$ films by recording high-resolution STEM ABF micrographs at the interface and close to the surface, which were vertically aligned at a nearly identical lateral position. Registered STEM datasets were recorded with an aberration corrected electron probe allowing for the unambiguous

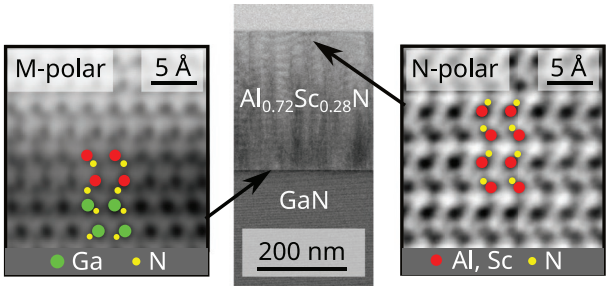

Figure 11. Registered and Gaussian-filtered STEM ABF micrographs of the 300 nm $Al_{0.72}Sc_{0.28}N$/GaN heterostructure in [11–20] zone axis. The structure is M-polar at the interface and N-polar close to the surface. The respective positions of the recorded micrographs are indicated by arrows. On the schematic models green dots depict Ga atoms, red dots Al/Sc atoms and yellow dots N atoms.

determination of $Al_{0.72}Sc_{0.28}N$ unit cell polarity at the atomic scale.[24] Although growing epitaxially, the nanoscale grain sizes and in-plane mosaicity of the investigated film implicated a challenging task for high-resolution STEM investigation. The small grain size causes overlapping orientations and irregularities in the field of view. Therefore, ABF as a very orientation angle sensitive technique resulted in unambiguous results only in certain regions.

The registered ABF datasets showing the atomic structure at the interface and at the top film region are presented in **Figure 11**, respectively. At the interface to the M-polar GaN buffer layer, the atomic structure of $Al_{0.72}Sc_{0.28}N$ exhibits also an M-polar configuration, which is illustrated by the schematics indicating the atomic species on their respective lattice positions. Conversely, the investigation of the relaxed region close to the surface revealed an N-polar structure.

Hence, the localized observations of position-dependent polarities in the $Al_{0.72}Sc_{0.28}N$ film confirm our initial hypothesis that the competition between an M-polar template and a deposition process that favors N-polar films leads to a transition between the polarities once a certain film thickness is reached. However, even with this initial multi-domain state, a single domain configuration can be obtained by either electrically polarizing the material or by keeping the film thicknesses below 30 nm.

5. Conclusion

Epitaxial ferroelectric $Al_{1-x}Sc_xN$ films with 19, 24 as well as 28 at% Sc and thicknesses ranging from 300 nm down to 10 nm were grown by sputter epitaxy on doped n-GaN/Al_2O_3 substrates. XRD, RSM, and pole-figures confirmed epitaxial growth and the expected [1–100](0001)$Al_{1-x}Sc_xN$ ‖ [1–100](0001) GaN relationship. At Sc concentrations above 19 at% the $Al_{1-x}Sc_xN$ lattice divides into a fully strained regime at the GaN interface and a relaxed regime above. Relaxation was further investigated combining aberration-corrected STEM and scanning NBED resulting in a strain map representing the whole thickness of the 300 nm $Al_{0.72}Sc_{0.28}N$ film. The aforementioned investigations reveal that $Al_{0.72}Sc_{0.28}N$ films up to ≈40 nm thickness are fully strained to the GaN, while for thicker films the

© 2022 The Authors. Advanced Functional Materials published by Wiley-VCH GmbH

extent of the fully strained regime is decreasing with increasing film thickness.

By reducing the Sc concentration from 28 to 19 at%, lattice-matched growth conditions can be obtained that result in a more uniform strain state throughout the films. From the electrical response, it was found that two ferroelectric displacement current peaks appear for films with thicknesses >30 nm and Sc concentrations > 19 at%. This indicates that this distinct switching behavior is related to the respective strain states inside films consisting of a fully strained as well as a more relaxed volume. The compressively strained volume close to the GaN interface is expected to switch at higher coercive fields, while the relaxed volume distant from the GaN interface is expected to switch at lower coercive fields. The initial polarization state of all epitaxial $Al_{0.72}Sc_{0.28}N$ films investigated in this study was proven by electrical measurements to be M-polar near the interface up to ≈30 nm film thickness with a subsequent transition to N-polarity. In contrast to the double-switching phenomenon, this is not related to different strain regimes, but rather due to the competing influence of the M-polar GaN template and the sputter process for $Al_{1-x}Sc_xN$ favoring N-polarity. Hence two polarities are present also in the lattice-matched $Al_{0.81}Sc_{0.19}N$ films. STEM ABF imaging as well as the results of etching experiments confirmed the conclusions obtained from the electrical measurements: M-polarity in $Al_{0.72}Sc_{0.28}N$ was found near the GaN interface due to the impact of the M-polar template, while near the surface N-polar $Al_{0.72}Sc_{0.28}N$ was confirmed. Our results therefore give a conclusive overview regarding the effect of epitaxial growth on the ferroelectric response of heterostructures containing III-N based ferroelectrics and help to advance the pending integration of ferroelectric functionality to III-N technology.

6. Experimental Section

The substrates consisting of a 4.5 µm Si-doped epi-GaN top-layer and its corresponding buffer layers grown on Al_2O_3 (0002) were commercially bought. The dopant concentration was specified as $\geq 10^{18}$ cm^{-3} and the resistivity was specified as < 0.5 Ω cm. The as-grown 4-in. n-GaN wafers were protected by a photoresist and diced into 1 × 1 cm^2 pieces. Prior to deposition, the pieces were cleaned with acetone and isopropanol in an ultrasonic bath followed by rinsing in DI-water. The $Al_{1-x}Sc_xN$ films as well as the Pt top-electrodes were grown by sputter deposition in an Oerlikon (now Evatec) MSQ 200 multisource system. The $Al_{1-x}Sc_xN$ films were deposited by reactive pulsed DC co-sputtering at 450 °C and a nitrogen flow of 15 sccm. More details about the process are described elsewhere.[12,28] All electrically characterized samples were capped with 100 nm of Pt after a preceding vacuum break to clean the Pt-target. The top-electrodes were structured with lithography and ion beam etching (IBE, Oxford Instruments Ionfab 300). The n-GaN served as bottom-electrode by contacting it via applying a silver conductive paste. Etching experiments were conducted on 100 nm thick $Al_{0.72}Sc_{0.28}N$ samples with sputter-deposited 30 nm Cr and 10 nm Au capping in a von Ardenne CS730S sputtering tool. The electrodes were structured with lithography and wet-etched with a KI/I_2 solution (Au) and TechniEtch Cr01 (Cr). After switching certain pads to full N-polarity, the top-electrodes were removed using the aforementioned etchants followed by etching in 85% H_3PO_4 at 80 °C. The sample topography (see Figure S7, Supporting Information), especially the occurrence of non-*c*-axis oriented protruding grains as described in previous publications,[28,29] as well as the etched samples were analyzed using a scanning electron microscope (SEM, Zeiss GeminiSEM). The Sc content was determined by SEM energy dispersive X-ray spectroscopy (EDS, Oxford x-act) at 13 kV. XRD measurements were performed using a Rigaku SmartLab diffractometer (9 kW, $Cu_{K\alpha}$ = 1.5406 Å, Hypix detector). The in-plane lattice parameters were extracted from the asymmetric 10–15 reflection. The pole figure was measured with a 2-dimensional X-ray detector configuration, at a center $2\theta/\omega$ angle of 65° and a center χ angle of 30°. With these settings, the {01–13} family of reflections of the $Al_{1-x}Sc_xN$ and GaN films, as well as the {01-18} family of the sapphire substrate was detected. The high-resolution reciprocal space maps were recorded with a 0.5° Parallel Slit Analyzer on the detector side. Ferroelectric measurements were performed using an AixACCT TF Analyzer 2000. The longitudinal thin-film piezoelectric coefficient $d_{33,f}$ was measured using an AixACCT double beam laser interferometer (DBLI) with a signal amplitude of 30 V at 711 Hz. The strain response in dependence of the electric field was measured with the same setup. Capacitance over electric field measurements were conducted on a Hewlett Packard 4284A Precision LCR meter with a small signal of 1 V peak to peak at 100 kHz sweeping 1 V steps with a delay of 500 ms between each step. A cross-section specimen of the as-deposited 300 nm $Al_{0.72}Sc_{0.28}N$/n-GaN film was prepared for local nanostructure analysis by performing a standard focused ion beam (FIB) procedure on a FEI Helios NanoLab G3 FIB-SEM Dualbeam system. Special care has been taken to minimize damage and Gallium implantation into the structure and to prevent material re-deposition at the interfaces of interest during the final 5 and 2 keV cleaning steps. High-resolution scanning transmission electron microscopy (HRSTEM) capable of directly visualizing a projection of the atomic structure was performed on a Nion HERMES microscope operated at 200 kV (convergence semi-angle of 25 mrad) with aberration-correction up to 5th order, achieving a theoretical point resolution of 0.06 nm. In order to investigate the atomic structure, especially to visualize the positions of the lighter element N that determines the polarity of the material, the annular bright field (ABF) imaging mode was used, collecting the scattering regime of roughly 15–30 mrad on an annular scintillator detector. To reduce noise and the influence of sample drift during image acquisition, series of ABF micrographs from a given sample area have been recorded, rigidly registered, then summed into a single image and finally subjected to a small Gaussian blur filter. To calculate the strain distribution, a scanning nano-beam diffraction map was acquired with 200 × 200 scan points over a 400 × 400 nm^2 area and a convergence angle of ≈0.3 mrad. A 50 × 200 portion of the data was processed with a homemade DigitalMicrograph script to obtain the strain maps calculated from the diffraction spot distances for each scan point. Prior to STEM investigations, the specimen has been baked overnight at 120 °C in a high vacuum to remove residual hydrocarbons that can impair the investigation. This temperature was not high enough to lead to relaxation mechanisms in the material.[30]

Supporting Information

Supporting Information is available from the Wiley Online Library or from the author.

Acknowledgements

This work was supported by the project "ForMikro-SALSA" (Grant no. 16ES1053) from the Federal Ministry of Education and Research (BMBF) and the Deutsche Forschungsgemeinschaft (DFG) under the scheme of the collaborative research centers (CRC) 1261 and 1461.

Open Access funding enabled and organized by Projekt DEAL.

Conflict of Interest

The authors declare no conflict of interest.

© 2022 The Authors. Advanced Functional Materials published by Wiley-VCH GmbH

Data Availability Statement

The data that support the findings of this study are available from the corresponding author upon reasonable request.

Keywords

aluminum-scandium-nitride ($Al_{1-x}Sc_xN$), epitaxial growth, ferroelectric, gallium nitride, semiconductors

Received: December 15, 2021
Revised: January 20, 2022
Published online: February 12, 2022

[1] (Eds.: K. Takahashi, A. Yoshikawa, A. Sandhu), *Wide Bandgap Semiconductors*, Springer, Berlin, Heidelberg **2007**.
[2] S. Nakamura, T. Mukai, M. Senoh, *Appl. Phys. Lett.* **1994**, *64*, 1687.
[3] U. Mishra, S. Likun, T. Kazior, Y.-F. Wu, *Proc. IEEE* **2008**, *96*, 287.
[4] J. Millan, P. Godignon, X. Perpina, A. Perez-Tomas, J. Rebollo, *IEEE Trans. Power Electron.* **2014**, *29*, 2155.
[5] M. T. Hardy, B. P. Downey, N. Nepal, D. F. Storm, D. S. Katzer, D. J. Meyer, *Appl. Phys. Lett.* **2017**, *110*, 162104.
[6] M. Zhu, E. Matioli, in *Proc. IEEE 30th Int. Symp. on Power Semiconductor Devices and ICs (ISPSD)*, **2018**.
[7] N. Chowdhury, Q. Xie, M. Yuan, K. Cheng, H. W. Then, T. Palacios, *IEEE Electron Device Lett.* **2020**, *41*, 820.
[8] T. Takeuchi, S. Sota, M. Katsuragawa, M. Komori, H. Takeuchi, H. Amano, I. Akasaki, *Jpn. J. Appl. Phys.* **1997**, *36*, L382.
[9] O. Ambacher, J. Smart, J. R. Shealy, N. G. Weimann, K. Chu, M. Murphy, W. J. Schaff, L. F. Eastman, R. Dimitrov, L. Wittmer, M. Stutzmann, W. Rieger, J. Hilsenbeck, *J. Appl. Phys.* **1999**, *85*, 3222.
[10] F. Tasnádi, B. Alling, C. Höglund, G. Wingqvist, J. Birch, L. Hultman, I. A. Abrikosov, *Phys. Rev. Lett.* **2010**, *104*, 137601.
[11] S. Zhang, D. Holec, W. Y. Fu, C. J. Humphreys, M. A. Moram, *J. Appl. Phys.* **2013**, *114*, 133510.
[12] S. Fichtner, N. Wolff, F. Lofink, L. Kienle, B. Wagner, *J. Appl. Phys.* **2019**, *125*, 114103.
[13] J. Hayden, M. D. Hossain, Y. Xiong, K. Ferri, W. Zhu, M. V. Imperatore, N. Giebink, S. Trolier-McKinstry, I. Dabo, J.-P. Maria, *Phys. Rev. Mater.* **2021**, *5*, 044412.
[14] P. Wang, D. Wang, N. M. Vu, T. Chiang, J. T. Heron, Z. Mi, *Appl. Phys. Lett.* **2021**, *118*, 223504.
[15] N. Grandjean, J. Massies, P. Vennéguès, M. Laügt, M. Leroux, *Appl. Phys. Lett.* **1997**, *70*, 643.
[16] S. Zhang, W. Y. Fu, D. Holec, C. J. Humphreys, M. A. Moram, *J. Appl. Phys.* **2013**, *114*, 243516.
[17] S. Fichtner; G. Schönweger; T.-N. Kreutzer; A. Petraru; H. Kohlstedt; F. Lofink, B. Wagner, in *Proc. 2020 IEEE ISAF*, **2020**.
[18] R. Meyer, R. Waser, K. Prume, T. Schmitz, S. Tiedke, *Appl. Phys. Lett.* **2005**, *86*, 142907.
[19] G. A. Jeffrey, G. S. Parry, R. L. Mozzi, *J. Chem. Phys.* **1956**, *25*, 1024.
[20] H. Schulz, K. Thiemann, *Solid State Commun.* **1977**, *23*, 815.
[21] S. Yasuoka, T. Shimizu, A. Tateyama, M. Uehara, H. Yamada, M. Akiyama, Y. Hiranaga, Y. Cho, H. Funakubo, *J. Appl. Phys.* **2020**, *128*, 114103.
[22] K. H. Ye, G. Han, I. W. Yeu, C. S. Hwang, J.-H. Choi, *Phys. Status Solidi RRL* **2021**, *15*, 2100009.
[23] D. Zhuang, J. Edgar, *Mater. Sci. Eng., R* **2005**, *48*, 1.
[24] N. Wolff, S. Fichtner, B. Haas, M. R. Islam, F. Niekiel, M. Kessel, O. Ambacher, C. Koch, B. Wagner, F. Lofink, L. Kienle, *J. Appl. Phys.* **2021**, *129*, 034103.
[25] P. Jiang, Q. Luo, X. Xu, T. Gong, P. Yuan, Y. Wang, Z. Gao, W. Wei, L. Tai, H. Lv, *Adv. Electron. Mater.* **2020**, *7*, 2000728.
[26] M. Stutzmann, O. Ambacher, M. Eickhoff, U. Karrer, A. L. Pimenta, R. Neuberger, J. Schalwig, R. Dimitrov, P. Schuck, R. Grober, *Phys. Status Solidi B* **2001**, *228*, 505.
[27] M. Si, X. Lyu, P. D. Ye, *ACS Appl. Electron. Mater.* **2019**, *1*, 745.
[28] S. Fichtner, N. Wolff, G. Krishnamurthy, A. Petraru, S. Bohse, F. Lofink, S. Chemnitz, H. Kohlstedt, L. Kienle, B. Wagner, *J. Appl. Phys.* **2017**, *122*, 035301.
[29] C. Sandu, F. Parsapour, D. Xiao, R. Nigon, L. Riemer, T. LaGrange, P. Muralt, *Thin Solid Films* **2020**, *697*, 137819.
[30] M. R. Islam, N. Wolff, M. Yassine, G. Schönweger, B. Christian, H. Kohlstedt, O. Ambacher, F. Lofink, L. Kienle, S. Fichtner, *Appl. Phys. Lett.* **2021**, *118*, 232905.

© 2022 The Authors. Advanced Functional Materials published by Wiley-VCH GmbH